Materials & Design 259 (2025) 114749

Contents lists available at ScienceDirect

Materials & Design

journal homepage: www.elsevier.com/locate/matdes

Bonding of vanadium- and Iron-based alloys as interlayers for plasma-facing and structural materials in fusion systems[1]

Tim Gräning [a,*], Deniz Ebeperi [b], Ibrahim Karaman [b], Ishtiaque Robin [c], Mobashera Saima Haque [d], Akhil Kolanti [d], David Sprouster [d], Lance Snead [d], Yutai Katoh [a]

[a] Material Science and Technology Division, Oak Ridge National Laboratory, Oak Ridge, TN 37831, USA
[b] Department of Materials Science and Engineering, Texas A&M University, College Station, TX 77843, USA
[c] Pacific Northwest National Laboratory, Richland, WA 99354, USA
[d] Department of Materials Science and Chemical Engineering, Stony Brook University, Stony Brook, NY 11794, USA

ARTICLE INFO

Keywords:
Additive manufacturing
Plasma-facing material
Vanadium
Functionally Graded Materials
Direct Energy Deposition
Fusion materials

ABSTRACT

Vanadium alloys and FeCrAl were investigated as interlayers between tungsten and reduced activation ferritic martensitic steel for fusion system components to avoid formation of intermetallic phase at operating temperatures between 550 and 1100 °C, while maintaining a body centered cubic phase throughout the interface. Physical and mechanical properties need to be graded between tungsten and steel, but recent results showed a significant hardness increase at the FeCrAl to vanadium alloy interface. Here, a sintered sample of these alloys was annealed for extended time, and the microstructure was investigated to provide a better understanding of the phenomena. A comparison with an additively manufactured interface of the same material is provided. An unexpected $L2_1$ intermetallic phase formation has been revealed using microscopy and synchrotron techniques and will inform future additive manufacturing approaches of the interface. A Cr layer interface as a preliminary solution was proposed between the Vanadium alloy and FeCrAl alloy interface.

1. Introduction

Tungsten is a promising candidate as the plasma facing material (PFM) in future fusion systems [1–3]. It can serve as an armor material, able to withstand the hazardous conditions inside current fusion power designs, including neutron irradiation and multiple million degrees Celsius in the plasma. These conditions result in high heat fluxes and transients at the first wall and divertor material. Tungsten exhibits excellent erosion resistance, high thermal conductivity, and moderate long-term neutron activation [4]. The PFM needs to be joined with structural materials like steel, while considering the large mismatch in the coefficient of thermal expansion (CTE; tungsten: 4.2 to 4.5 x 10^{-6} K^{-1} at room temperature (RT) [5–7], ferritic steel at RT: 14.8 x 10^{-6} K^{-1} [8]). A direct or functionally graded joint between tungsten and reduced activation ferritic martensitic (RAFM) steel is possible using sintering, plasma spraying or additive manufacturing. However, the Fe-W binary phase diagram suggests that the interface is likely to form a significant amount of brittle intermetallic phases such as Fe_2W or Fe_7W_6 during operation [9,10].

Previous thermodynamic simulations suggested an interlayer design transitioning from RAFM steel to FeCrAl, to VCrAl, to VCrTi (or pure V) and finally to tungsten to avoid brittle intermetallic phases across the interface. The simulation predicted the formation of a stable body-centered cubic lattice structure across the interlayers, within the targeted operating temperature regime of 550 °C and 1100 °C [11]. A spark plasma sintering (SPS) method of those interlayers was used to

[1] Notice: This manuscript has been authored by UT-Battelle, LLC, under contract DE-AC05-00OR22725 with the US Department of Energy (DOE). The US government retains and the publisher, by accepting the article for publication, acknowledges that the US government retains a nonexclusive, paid-up, irrevocable, worldwide license to publish or reproduce the published form of this manuscript, or allow others to do so, for US government purposes. DOE will provide public access to these results of federally sponsored research in accordance with the DOE Public Access Plan (https://www.energy.gov/doe-public-access-plan).

* Corresponding author.
E-mail addresses: graeningt@ornl.gov (T. Gräning), ebeperi@tamu.edu (D. Ebeperi), ikaraman@tamu.edu (I. Karaman), ishtiaquekarim.robin@pnnl.gov (I. Robin), mobasherasaima.haque@stonybrook.edu (M.S. Haque), akhil.kolanti@stonybrook.edu (A. Kolanti), david.sprouster@stonybrook.edu (D. Sprouster), lance.snead@stonybrook.edu (L. Snead), katohy@ornl.gov (Y. Katoh).

https://doi.org/10.1016/j.matdes.2025.114749
Received 26 June 2025; Received in revised form 21 August 2025; Accepted 10 September 2025
Available online 19 September 2025

manufacture a sample to investigate the formed interfaces, revealing a significant hardness and elastic modulus change at the FeCrAl to VCrAl interface [11]. This change of mechanical properties was previously attributed to vanadium carbide formation, as extensive XRD analysis did not detect any intermetallic phases across that interface.

To further investigate the phenomena, an in-depth microstructure characterization was performed at the VCrAl − FeCrAl interface of an annealed SPS sample. The objective is to elucidate the underlying cause of the previously reported abrupt change in mechanical properties at this interface. Additionally, the effects of similar property discontinuities in a laser-beam directed energy deposition (LB-DED) build are discussed. The insights gained will provide guidance and raise awareness to the community regarding the challenges of joining vanadium and iron alloys for fusion system applications.

2. Experimental procedures

Tungsten and VCrTi discs with a thickness of around 1 mm were bonded first at 1200 °C using 10 MPa and subsequently bond together with VCrAl, FeCrAl and RAFM at 1100 °C using 10 MPa with a holding time of five minutes. More details regarding the SPS manufacturing parameters using are described elsewhere [11]. This study focusses specifically on the FeCrAl to VCrAl interface. The chemical compositions of FeCrAl and VCrAl as determined by inductively coupled plasma mass spectroscopy (ICP-MS) and CNO analyzer are shown in Table 1 for the SPS and the additively manufactured sample.

The SPS sample was annealed at a targeted temperature of 620 °C for 1000 h in an Ar-backfilled glass vial. This temperature was chosen to simulate the maximum operating temperature anticipated for the designed interface in a fusion power system. The diffusion parameters for this sample were recently reported [12]. Here, annealing helps to extend the diffusion distance, making the investigation easier.

To test the printability of this interface, LB-DED technique was chosen to fabricate multi-material systems. LB-DED excels for multi-material systems in comparison to other additive manufacturing (AM) techniques. Pre-alloyed FeCrAl and VCrAl rods were gas atomized to produce spherical powders (45-106um PSD) for LB-DED at Nanoval GmbH & Co. KG (Berlin, Germany). Deposition was performed using an Optomec LENS MR-7 powder-fed LB-DED system, equipped with an IPG Nd:YAG 1 kW continuous wave coaxial laser and four powder feeder chambers. The process was conducted under ultra-high purity (>99.995 %) Ar atmosphere maintaining oxygen levels between 10–50 ppm. LB-DED processing parameters for both FeCrAl and VCrAl alloys were optimized following a comprehensive parameter optimization framework [13]. To fabricate the transition interface, the layer thickness (LT) of both alloy layers were determined based on single-track experiments and an LT criterion developed for LB-DED [14]. Four layers of FeCrAl with a layer thickness of 366 μm were deposited over eight layers of VCrAl with a layer thickness of 158 μm, resulting in a diffusion driven interface between the two materials. A laser power of 380 W, a scan speed of 5 and 9 mm/s, a powder feeder rotary speed of 2 and 4, and a hatch spacing of 650 and 428 μm were used for FeCrAl and VCrAl deposition, respectively.

The manufactured SPS and LB-DED samples were embedded and metallographically polished to a sub-micron finish. Subsequently, scanning electron microscopy (SEM) was performed using a MIRA 3 SEM by TESCAN USA, Inc. equipped with an Oxford Symmetry EBSD detector using a probe current of around 4nA. EBSD data were collected at an accelerating voltage of 20 kV and beam current of 6nA with step sizes of 0.2 μm for all scans. For TEM sample preparation, two grains close to a (100) and (110) zone axis-orientated normal to the sample surface across the interface- were selected as a preferred lift-out location. Focused Ion Beam (FIB) preparation of a lamella of around 12 μm across the FeCrAl and VCrAl interface from the SPS sample was conducted and subsequently thinned to a thickness of around 120 nm in the regions of interest. TEM was performed using a FEI (now Thermo Fisher Scientific, Waltham, MA, USA) Talos F200X scanning transmission electron microscope operating at 200 kV. Energy dispersive X-ray spectroscopy (EDS) was used to map element distributions and observe chemical variations across the interfaces. Mappings were completed using a probe current of ~ 1nA and a probe size of less than 1 nm with active drift correction every 20 s. The spectrum images were recorded using a 1024 × 1024 pixels region with a 2px gaussian averaging filter applied during image post-processing. Atomic number, absorption, and fluorescence (ZAF) corrections were performed to extract atomic compositions. Line scans were conducted on the raw data of mappings. An error value for scanning transmission electron microscopy (STEM) EDS values is assumed to be 3 percent, but the reader should be aware that the applied ZAF correction is an approximate correction method and that shadowing, absorption effects, sample thickness effects, and statistical error in the background subtraction are possible. In addition, Al is sensitive to beam damage and can migrate or be sputtered during long STEM-EDS scans [15]. Nanoindentation testing was performed in a TESCAN MIRA3 SEM using a Nanomechanics InForce 1000 actuator with a diamond Berkovich tip with a step size of 2 μm focusing on the measurement of mechanical properties changes across the interface. 40 indentations per x-position were recorded using NanoBlitz3D mapping software with more details on the method published elsewhere [11,16].

XRD measurements were performed at the National Synchrotron Light Source-II (NSLS-II) using the high-energy X-rays available at The Pair Distribution Function (PDF) beamline. All measurements were performed in transmission mode with an amorphous Silicon-based flat panel detector (Perken-Elmer) mounted orthogonal to and centered on the beam path. The sample-to-detector distances and tilts of the detector relative to the beam were refined using a LaB_6 powder standard (NIST standard reference material 660c). The wavelength of the incident X-rays was 0.1665 Å (74.46 keV). The sample-to-detector distance was calculated to be 999.35 mm. 100 XRD patterns were collected and averaged with detector exposures of 0.1 s. Specimens were horizontally scanned across the different layers with a 300 μm step size. All raw two-dimensional patterns were corrected by subtracting a dark current image, and the air and Kapton scattering background within IgorPro (Wavemetrics) software [17]. Noticeable artefact regions of the detector (like the beam stop, dead pixels) were masked. The corrected and masked two-dimensional detector images were then radially integrated to obtain one-dimensional powder diffraction patterns.

The background subtracted XRD patterns were loaded into MATCH!3 for phase identification and subsequently refined within the MAUD software package [18]. The instrument contribution to the broadening of the measured profiles was quantified by fitting the LaB_6 NIST powder standard, with a known coherent grain size and negligible microstrain contribution. The Gaussian and Lorentzian-based broadening parameters were subsequently fixed during the analysis of the alloys under investigation to quantify the microstructure. The lattice parameters and

Table 1
Chemical composition of FeCrAl and VCrAl alloys used in this study in weight percentage.

Material		Fe	V	Cr	Al	Ti	O	C
FeCrAl	SPS	Bal.	–	10.46 ± 0.07	10.86 ± 0.18	0.11 ± 0.01	0.01	0.03
	DED	Bal.	–	8.80 ± 0.07	7.38 ± 0.09	0.11 ± 0.01	0.003	–
VCrAl	SPS	–	Bal.	11.24 ± 0.08	11.67 ± 0.19	0.09 ± 0.01	0.08	0.05
	DED	–	Bal.	14.52 ± 0.25	7.17 ± 0.19	0.09 ± 0.01	0.12	–

microstrain were refined for the Fe and V phases, with additional texture (arbitrary texture) included in the XRD refinements. Such inclusion prohibits phase fraction determination; however, the strength of the XRD peaks of the minor phases is sufficient to achieve a semi-quantification. The lattice parameters and coherent grain size were allowed to vary for the minor crystal phases present. A polynomial background was included in the refinements to capture the diffuse background.

3. Results

Fig. 1 displays a hardness and elastic modulus (E-Modulus) plot next to the SEM EDS map in atomic percentage (wt.%) of the major elements. The same x-position across the FeCrAl and VCrAl interface was used for both measurements. The nanoindentation mappings show the gradual increase in hardness and elastic modulus over 45 μm from FeCrAl side towards the VCrAl layer. The mechanical properties exhibit a sudden drop after reaching a maximum value at around 85 to 90 μm on the x-position. The hardness increases from around 5 to 8 GPa and then drops to the 5.5 GPa.

The E-Modulus over the same distance increases from 210 GPa in FeCrAl to 270 GPa at the 85-μm x-position and drops to around 200 GPa in the VCrAl material. The distance with a measurable mechanical properties increase spans from the 50 to 90-μm x-position, which coincides with the diffusion area of Fe and V shown in the SEM-EDS line scan in Fig. 1b. A FIB lamella was extracted from the 78 to the 90 μm x-position and is highlighted by the gray area in Fig. 1 and as a black bar in the inverse pole figure (IPF) map in Fig. 2a. The left side of the IPF map in green with $< 011 >$ grains represents the region of FeCrAl, and the right side $< 111 >$ oriented grains represent VCrAl. The IPF map is evaluated in the direction of the FIB liftout and the chemical gradient (left to right/ x-direction).

Fig. 2b shows a STEM HAADF map, overlayed with an EDS map of Fe (yellow) and V (pink) visualizing the chemical gradient. The regions presented with circles 1 to 5 were used for selected area electron diffraction (SAED), and areas with circles 2 and 3 were used for HR-TEM. Region 1 is within the [011] zone axis (ZA) oriented grain displayed in the IPF map in Fig. 2a (green colored grain). Regions 2 to 4 are inside the [001] ZA oriented grain at the interface (red colored grain), and region 5 in the original VCrAl layer (blue colored grain), tilted to a [001] ZA. Tilting to either [001] or [011] ZA was conducted to make potential superlattice diffraction visible. Those superlattice positions were found for SAED positions 1 to 3, shown at the bottom of Fig. 2. The elemental line scan, shown in Fig. 2c, is taken across the line exhibited on the bottom of the STEM-EDS map in Fig. 2b.

The chemical compositions extracted from the linescans at the five SAED positions are summarized in Table 2. The Al content is underrepresented in the TEM EDS linescan in comparison with the SEM linescan and chemical analysis results shown in Table 1. Absorption effects from the grid, the sample itself, or carbon, can impact the analysis. It is assumed that the SEM EDS and chemical composition results are more precise. As predicted by thermodynamic simulations [11], there is only limited diffusion of Fe into the V matrix, but significant V diffusion into the Fe matrix. This results in a pronounced enrichment of Fe and V at the original bonding interface located at around 5-μm x-position in Fig. 2c, of the two layers. Fe diffusion is limited to 1 to 2 more microns inside V, while V content drops from 70 to 25 atomic percentage over 5 μm. It takes another 30 μm for the vanadium content to drop from 25 to 0 atomic percent, as shown in the EDS linescan in Fig. 1. Uphill diffusion of Cr at the interface, as predicted by Pandat simulations [11,12], was also observed but is not expected to significantly influence the mechanical properties.

Figs. 3a and b show two high-resolution (HR) bright field (BF) TEM micrographs with two higher magnification insets, taken from the respective regions (1 and 2, close to 1 and 4 μm on the linescan) shown in Fig. 2b. Despite compositional differences between these two regions, changing from 55at.% Fe and 27at.% V to 32at.% Fe and 45at.% V, the corresponding SAED patterns exhibit no discernible shift in diffraction positions or patterns. The recorded selected area electron diffraction pattern is shown in Fig. 3c, with the sample tilted close to a [001] zone axis (ZA). The dashed lines show the typical low-index diffraction pattern expected for an A2 lattice type. The yellow circles, however, highlight the existence of superlattice peaks, indicating an intermetallic phase formation. To identify the phase observed in Fig. 3c, the ICSD files of B2 Fe-Al [19], B2 Fe-V[20], Sigma Fe-Cr [21], Sigma Fe-V [22], $L2_1$ (Al0.5 V0.5) Fe [23], body-centered cubic (bcc) Fe [24], and V [25] were compared in SingleCrystal software. The pattern best matched $L2_1$ (Al0.5 V0.5) Fe with a lattice constant of 0.576 nm, confirming the formation of an intermetallic phase. However, σ Fe-V, and B2 (Fe-Al & Fe-V) also exhibit close agreement with a lattice parameters of 0.291 and 0.290 nm.

Although the formation of an intermetallic phase was confirmed, the results remain ambiguous, since both B2 (CsCl-type) phases (Fe-Al or Fe-V) and $L2_1$ phase have similar lattice constants and exhibit very similar diffraction positions when observed along the [0 0 1] ZA. To resolve this ambiguity, region 1 in Fig. 2 was tilted to a ⟨0 1 1⟩ ZA, and the corresponding diffraction pattern is shown in Fig. 4 next to the simulated diffraction patterns of previously mentioned phases, *i.e.*, B2, σ, and $L2_1$. Only the $L2_1$ phase in Fig. 4d fully matches the diffraction positions observed in Fig. 4a. That confirms that we certainly have the formation of the $L2_1$ phase. However, the additional presence of an overlapping B2 phases (Fe-Al or Fe-V) cannot be confirmed or excluded; a mixture of multiple phases is indeed possible and will be further addressed in the next section. Further, the σ Fe-V phase oriented along the [321] ZA

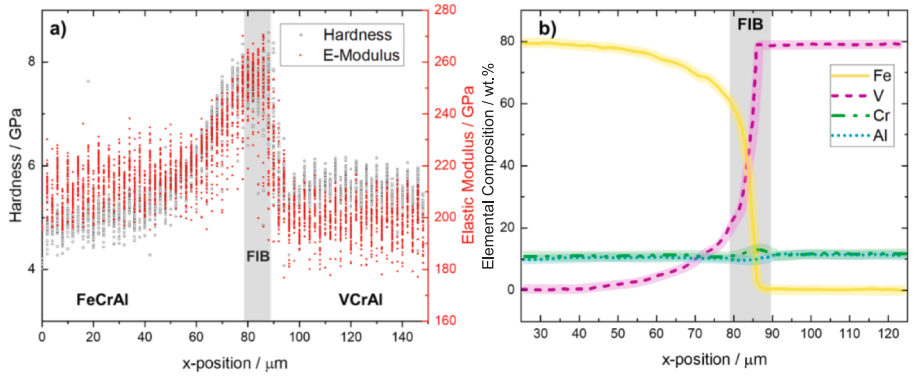

Fig. 1. A) hardness (open black square) and e-modulus (red circles) measured by nanoindentation are shown across the FeCrAl and VCrAl interface. b) Experimentally determined elemental composition via SEM-EDS of major elements is shown for the same x-positions as the nanoindentation mapping. An error of around ± 3 % is assumed from the mean values for the elemental compositions. The location of a FIB lamella liftout is highlighted.

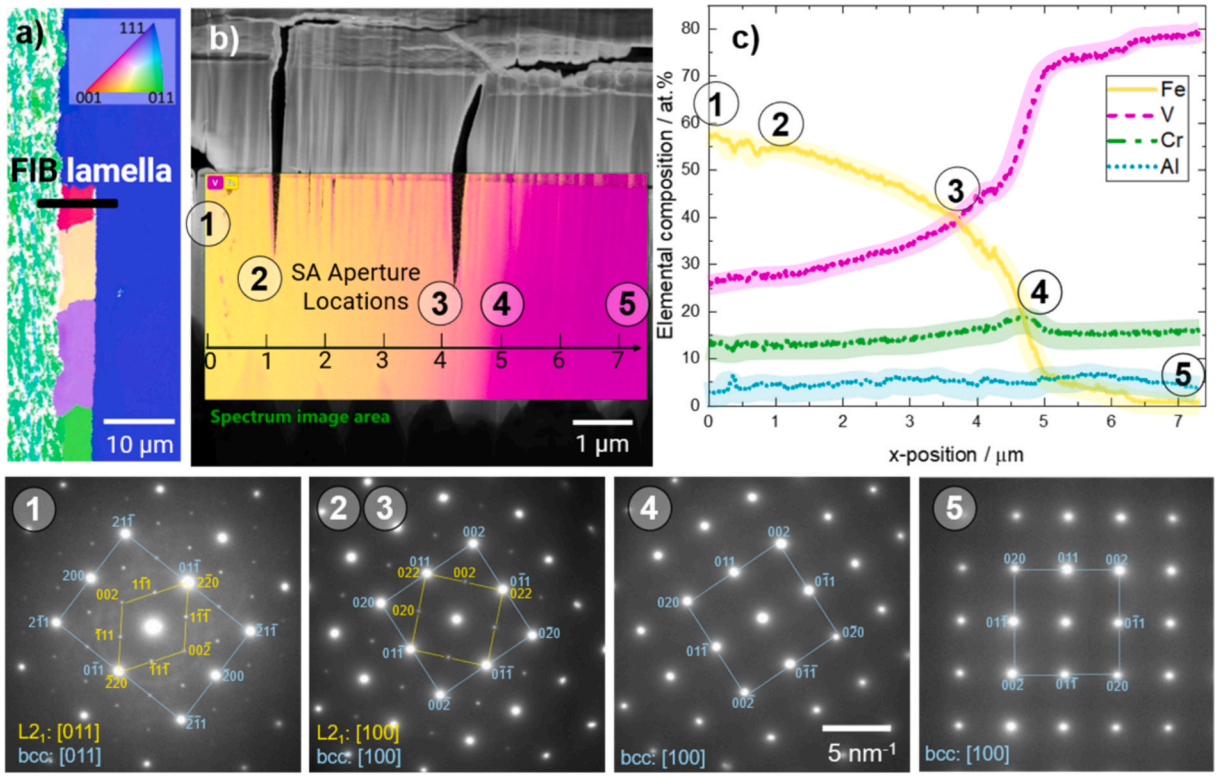

Fig. 2. a) IPF map of FeCrAl (left) and VCrAl (right) interface shows the targeted FIB lift-out location on a grain formed at the interface after annealing at 620 °C for 1000 h; b) STEM HAADF map overlayed with Fe (yellow) and V (pink) EDS map showing the five SA aperture locations with circled numbers and the line scan location; c) line scan across 7 µm reveals the diffusion profile of all major elements. The corresponding diffraction patterns extracted from the five SA locations are on the bottom.

Table 2
Approximate atomic weight percentages at the five SAED positions taken from the STEM-EDS line scan in Fig. 2.

SAED Position	1	2	3	4	5
Fe	58	55	36	17	0
V	25	27	43	62	80
Cr	13	13	16	16	16
Al	4	5	5	5	4

partially matches the observed diffraction pattern, although it exhibits greater deviation compared to the B2 and $L2_1$ phases.

A stitched STEM-EDS map of Cr (orange) is shown in Fig. 5, with yellow rectangles highlighting the location of the magnified Cr EDS map in the HAADF image on the top left. The reason to show the Cr EDS map is that the cell-like structure around the precipitates is more prominently visible. The average chemical composition across the area is shown on the bottom linescan in x-direction. A shorter line scan of 450 nm is highlighting the Cr-rich phase formation (arrows), clearly separated from the V and Al-rich phases. The inset figure of V of the marked region in the Cr EDS map shows the clear phase separation between the Cr-rich matrix and the V-rich precipitates. The cell size of the Cr-rich phase is increasing with a rising Fe and decreasing V concentration, as shown in the average linescan on the bottom of Fig. 5. Vice versa, the precipitate size of the vanadium-rich phase and the spatial separation between the two phases are decreasing with an increasing vanadium amount. A two-phase region is confirmed within the 25 to 33 at.% range of V. That area is represented by the 0 to 2.5 x-position of Fig. 2c which includes the SAED positions 1 and 2 shown in Fig. 2 and Table 2. Approximate atomic weight percentages at the five SAED positions taken from the STEM-EDS line scan in Fig. 2. and are shown Table 2. For vanadium contents higher than 33 at.%, no clear separation of phases is visible.

Fig. 6 shows the XRD patterns for SPS and LB-DED specimens. The dominant crystalline phases identified in both specimens include the bcc V and bcc Fe. Both specimens show peaks corresponding to the Fe-Al-V $L2_1$ phase, with visible peaks at 2.9 and 3.2 and 5.5 degrees. The peaks corresponding to the B2 phase only appear to be present in the LB-DED specimen. The similarity in the lattice parameters and identical crystal structures of the two FeV and AlFe B2 phases necessitates a phase quantification through XRD pattern refinements. No FeCr or FeV σ phase is observable in the two specimens' XRD patterns. It is noted that the peaks associated with the $L2_1$ phase in the LB-DED specimen are broad, indicative of small coherent grain sizes, while the peaks for the B2 phase are less broad (i.e., larger coherent grain sizes). The $L2_1$ peaks in the SPS sample are sharper than the LB-DED specimen, indicating these precipitates have larger coherent grain sizes.

Table 3 summarizes the phases and microstructures quantified from the XRD analysis. This table confirms the qualitative coherent grain size analysis discussed above for the two specimens. The lattice parameters of the $L2_1$ phase in both specimens are similar to the bulk phase. Similarly, the lattice parameters of the B2 phases are consistent with their corresponding bulk phases. The inclusion of a B2 phase in the analysis of the SPS sample's XRD pattern led to physically non-realistic values in lattice parameters and coherent grain sizes (<1nm), indicating that this phase is too low in fraction to be quantified or not present, consistent with the TEM results described above.

Both materials were fabricated via LB-DED, with FeCrAl deposited on top of VCrAl. An IPF map of the resulting structure is presented in Fig. 7a, along with the corresponding EDS maps showing the distribution of Fe and V in Fig. 7b. The IPF is evaluated along the build direction, revealing grain continuity across the diffusion area, characterized by elongated grains oriented in the build direction. Fig. 7c shows a kernel average misorientation (KAM) map, exhibiting stronger local grain misorientation perpendicular to the build direction. Crack formation is

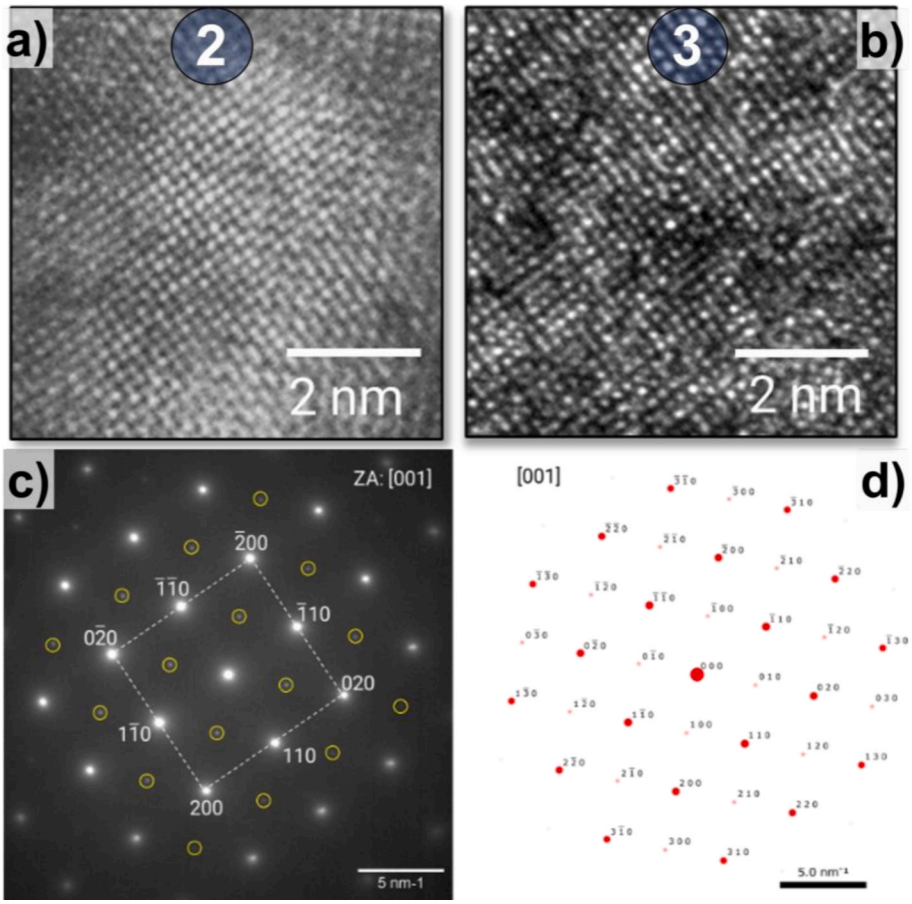

Fig. 3. a) and b) show high-resolution bright field images of SAED locations 2 and 3 shown in Fig. 2b; c) SAED pattern at both positions shows a 100 zone axis and marked with yellow circles forbidden positions for a Im3m lattice; d) simulated B2 Fe-V (as well as B2 Fe-Al and $L2_1$) pattern on the 100 zone axis matches with the diffraction pattern in c).

observed in the overlayed image quality (IQ) and IPF map in Fig. 7d in black, but also visible in the EDS and KAM map in Fig. 7b and Fig. 7c.

During the LB-DED process, the deposition of FeCrAl layers leads to partial and repetitive re-melting of the underlying VCrAl layers, promoting elemental interdiffusion and formation of the reaction layer shown in Fig. 7b. The thermal history within this diffusion zone is highly complex and requires further investigation using advanced characterization techniques, such as in-situ thermal monitoring and elemental interdiffusion simulations to accurately determine local temperature profiles and estimate the effective depth of elemental mixing and the anticipated phase constitution. The produced experimental data will be used in simulation efforts to align the produced microstructure with simulation efforts.

4. Discussion

Thermodynamic calculations and diffusion experiments for Fe and V at the FeCrAl and VCrAl interface have resulted in a diffusion distance of approximately 40 μm after 1000 h at 620 °C. This diffusion length matches the spatial extent of the mechanical property variation observed in Fig. 1 [12]. In an earlier study [12], it was hypothesized that carbide formation, due to the presence of carbon in both layers, was responsible for the observed increase in hardness. Although carbide formation can enhance mechanical properties, prior SEM observations of the interface confirmed that carbides were localized within 5 to 10 μm of the interface [12]. Therefore, carbide formation alone cannot explain the magnitude of the mechanical property changes observed across a 40-μm-wide region. The hardness and elastic modulus increase across this short distance can lead to catastrophic mechanical failure, caused by thermic cycling or heat flux transients during fusion reactor operation. Thermal cycling and fatigue are caused by an on-demand intermittent operation of a fusion power plant. The spike in mechanical properties makes the material susceptible to stress concentration and premature failure. As this interface is designed to serve between the plasma facing material and structural material, stress concentration would result in a critical leak of coolant. Fig. 2 shows a STEM image of the TEM lamella and the chemical gradient across the interface and clearly shows the formation of an intermetallic phase.

A comparison of the EDS linescan in Fig. 1 and Fig. 2 shows a significant difference in Al content between the SEM and the STEM EDS results. It is possible that shadowing, absorption effects, sample thickness effects, and statistical error in the background subtraction led to a difference in the measured Al content, but a careful evaluation was required. A possible explanation could be the formation of an aluminum-rich surface layer or the formation of oxides during the annealing. Even though the annealing has been performed in a quartz vial, which was purged with argon three times, a formation of Al oxides might have occurred, which was not observed in the small region of interest (ROI) in the TEM sample. As the bulk SEM EDS scan clearly showed that Al is measured close to the chemically measured weight percentage, a wrong chemical composition of the used materials can be ruled out. A STEM EDS map of an unannealed sample condition of the same interface was taken and exhibited an Al content of around 10 at%. That is still low in comparison to the SEM EDS percentages of around 18 at.%, but slightly higher than that of the annealed sample. The difference of 3 to 4 at.% of Al between the as-manufactured and the annealed SPS sample indicated the diffusion and formation of an Al-rich phase not shown in the ROI of the TEM sample. We found that a small amount of Al diffused to form an

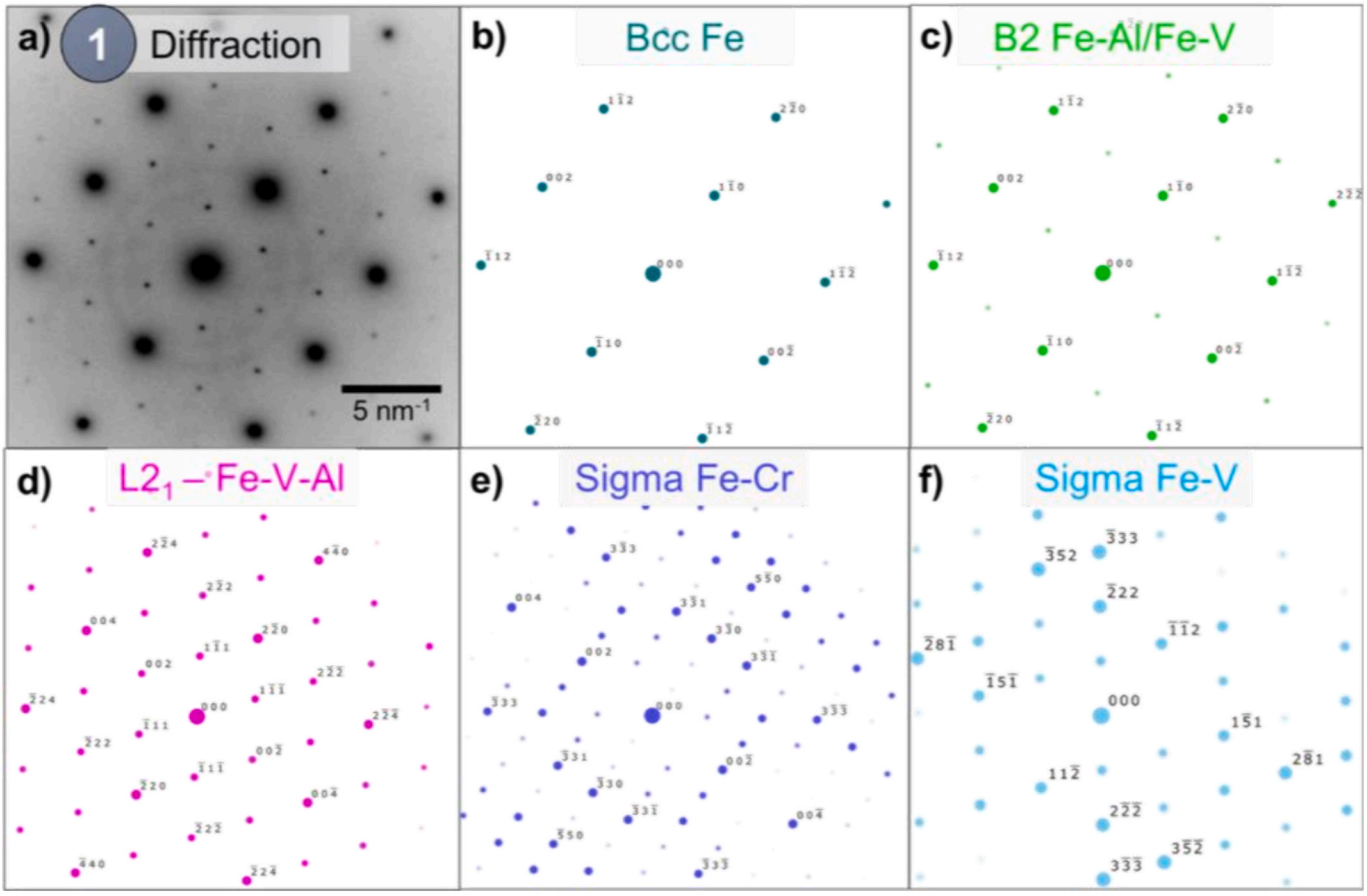

Fig. 4. A) inverted diffraction pattern close to the[110] ZA at SAED location 1 (shown in Fig. 2), next to simulated patterns of b) bcc Fe, c) B2, d) $L2_1$, e) σ Fe-Cr and f) σ Fe-V phases. Only the $L2_1$ phase in d) fully matches with the diffraction pattern in a).

enriched Al-phase at the sample surface outside the ROI in the TEM lamella. Additionally, differences in the low-kV final polish of the FIB sample preparation can lead to a difference between the annealed and the unannealed SPS sample, as TEM lamellae were produced by different operators. To summarize, we conclude that the annealed STEM-EDS lamella has formed an Al-rich surface layer outside the ROI and under-reports Al because the low-energy Al Kα (1.486 keV), which suffers significant self-absorption and detector shadowing in TEM geometry.

Fig. 2 presents five SAED patterns, the first of which is oriented close to a < 110 > ZA, clearly highlighting the presence of an $L2_1$ phase corresponding to the composition measured at SAED Position 1, as detailed in Table 2. To further identify the phases present, the experimental results are compared with phase diagrams available in the literature. Recently, Wang et al. optimized the thermodynamic database for the Fe-V-Al system, suggesting the formation of an $L2_1$ phase instead of a B2 phase for compositions with Al contents below 20 at. % at annealing temperatures below 700 °C. The measured chemical composition range within the entire TEM lamella (excluding Al, and Cr, respectively) is shown by the gray region in the Fe-V-Cr and Fe-V-Al ternary phase diagrams shown in Fig. 8. These phase diagrams, reproduced from the literature, correspond to annealing temperatures of 480/500 and 700 °C [26,27]. Based on these diagrams, the formation of a B2 (Fe-Al or Fe-V) phase as shown in Fig. 4 would not be expected under the operating conditions of the structural materials in plasma-facing components, which have an upper operating temperature around 700 °C. However, since any fabrication method (AM or other potential techniques) used to achieve the present chemical gradient would expose the interface to temperatures exceeding 700 °C, the formation of a B2 phase remains possible. In fact, Ferreiros et al. investigated the $Fe_{1-2x}Al_xV_x$ system and identified a stable high temperature B2 phase for Aluminum content above 10 at.% [29].

It is important to note that the Al concentrations reported in the STEM EDS map represent the minimum and maximum values measured via ZAF-corrected STEM EDS mapping and are lower than those obtained using chemical analysis and SEM EDS measurements. This systematic underestimation of Al in STEM EDS measurements is likely results from several effects described above and in the methods section; hence, the actual Al concentration can be assumed to be higher, as supported by the SEM EDS scans in Fig. 1b. The STEM EDS linescans and the Cr elemental map in Fig. 5 clearly indicate a 2-phase region at V contents between 20 and 33 at.%. The Cr-rich phase contains about 3 at. % of Al, while the V- and Al-rich phase shows reduced Cr levels about 5 at. %. Given the relatively low Cr and Al concentrations within these phases, the ternary phase diagrams Fe-V-Cr and Fe-V-Al shown in Fig. 8 can be used to deduce the phases formed. The experimentally observed phases are marked in all four ternary phase diagrams with red (Al-, and V-rich) and blue (Cr-rich) crosses. The Fe-V-Al ternary phase diagrams clearly indicate that the Al- and V-rich phase is an $L2_1$ phase, whereas the Cr-rich phase is either σ or α phase. Synchrotron XRD measurements in Fig. 6 agree with the TEM results, confirming the formation of an $L2_1$ phase together with a bcc phase, without a σ phase formation detected in either the SPS or DED samples.

The intrinsic high hardness of the $L2_1$ contributes substantially to the hardness increase. A single phase $L2_1$ phase region forms around 10 to 20 at.% Al, between 20 and 28 at.% V and Fe as balance at temperatures of 500 °C. Here, with the composition in the diffusion region being very close to that single phase region of the $L2_1$, the mechanical properties of the existing two-phase region should be very close to that of the pure $L2_1$ phase, assuming a rule of mixture of properties. Aside from the above-

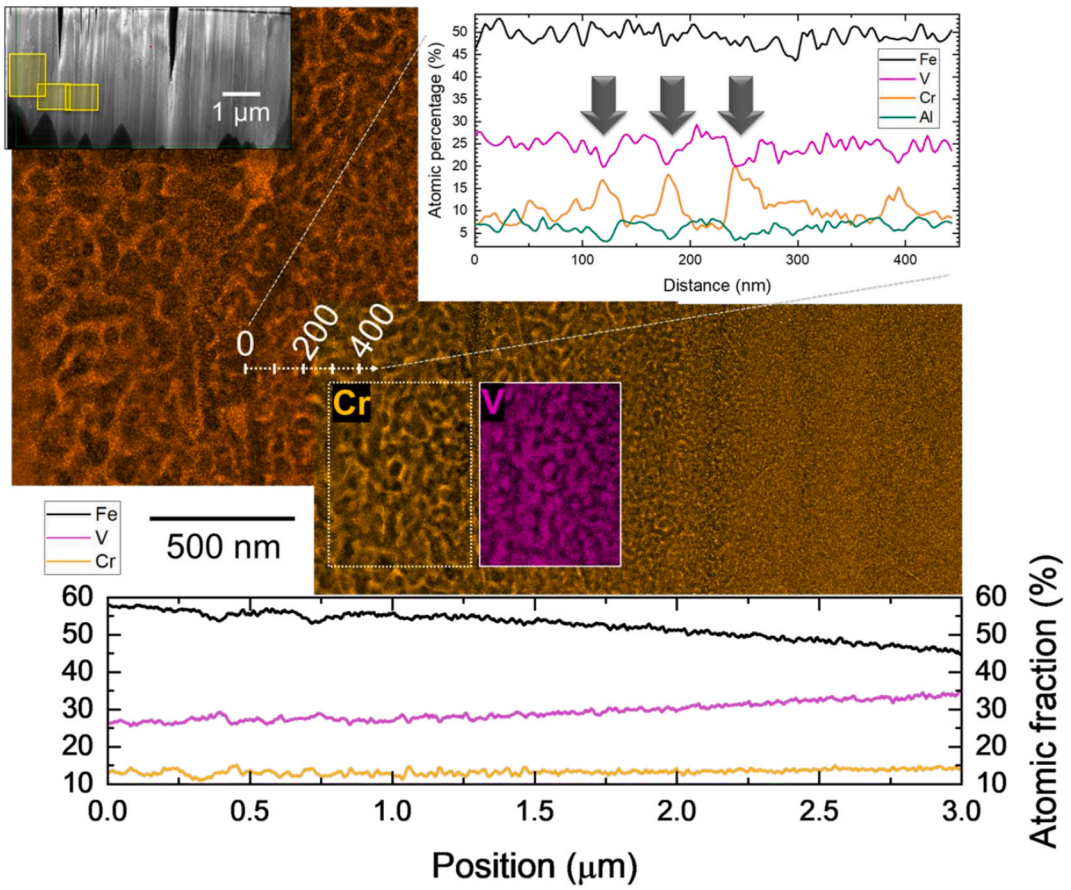

Fig. 5. Cr STEM-EDS map in orange from three stitched locations shown in the top left of the FIB lamella, together with a 450 nm linescan showing a two-phase region, with Cr, separating from a V- and Al-rich phase (arrows). Fe does not show any phase separation. A V STEM EDS inset is shown for the marked area and shows clearly the separation between the two phases. The line plot at the bottom shows the average chemical composition change from left to right with identical scaling as the EDS Cr map.

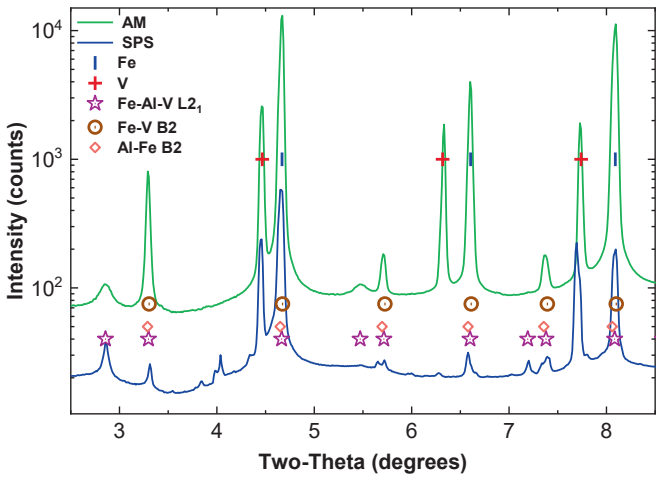

Fig. 6. Representative XRD patterns collected for the SPS and LB-DED specimens for a region that incorporates the FeCrAl to VCrAl interface. The phases identified are labeled with symbols for reference.

mentioned composition, a clear two-phase region has formed in the form of $L2_1$ precipitates, with a very high density of nano-scaled precipitates shown in Fig. 5. The finely dispersed $L2_1$ precipitates act as obstacles to the movement of dislocations, impeding their propagation and making it harder for the material to deform. The dominant strengthening mechanism is from precipitate strengthening with coherent precipitates.".

Based on the Fe-V-Al ternary phase diagrams, for the investigated alloys with an Al content between 3 and 10 at.%, the $L2_1$ phase is expected to form at temperatures between 500 and 700 °C with V content ranging from 5 to 55 at. %, balanced by Fe. Assuming a V fraction of around 55 at.% as the boundary condition to form $L2_1$, no $L2_1$ phase would be expected at the linescan x-position of 4.8 µm in the TEM samples presented in Figs. 2b and 2c. This is confirmed by the diffraction pattern of the SAED position 4, which does not show any intermetallic phase and aligns well with Wang's thermodynamic model [26].

However, examination of the HR TEM images in Fig. 3, recorded at SAED positions 2 and 3 within the two-phase region, does not identify if a second intermetallic phase formed together with the $L2_1$ phase. This uncertainty arises because the $L2_1$ and B2 phases exhibit a cube-on-cube orientation relationship with the ferritic matrix $<100>_{Intermetallic} \parallel <100>_{Fe\_\alpha}$ as shown in Fig. 3 and Fig. 4. leading to indistinguishable SAED patterns and HR TEM image contrasts. Here, using a negative spherical aberration coefficient (CS) corrected TEM could potentially improve phase differentiation, but would be preferred on a single composition sample, to eliminate ambiguities due to a likely chemical gradient. Even though, dark-field imaging using different diffraction $<111>$ g vectors of the [011] ZA could potentially aid in distinguishing between the different phases. The synchrotron XRD results show a clear abundance of the L21 phase, with no B2 phase found in the SPS sample. That made that distinction in TEM unnecessary for the SPS sample. From an application perspective, it does not matter which of the phases form, as both phases are embrittling and harmful for the component lifetime inside a fusion reactor. A dedicated single composition study with different cooling rates is recommended to distinguish between both

Table 3
Quantification of the microstructural results from the XRD analysis. a = lattice parameter, CGS = coherent grain size (nm) and μS = XRD microstrain.

Specimen	Phase	a (Å)	±	CGS (nm)	±	μS	±
LB-DED	Fe	2.89296	0.00012	–	–	0.0017	0.0001
	V	3.02303	0.00014	–	–	0.0012	0.0001
	L21	5.80835	0.00430	12.0	2.0		
	B2	2.88937	0.00030	420.8	20.0		
	B2	2.90090	0.00063	165.6	20.0		
SPS	Fe	2.89874	0.00015			0.0029	0.0000
	V	3.03563	0.00023			0.0020	0.0001
	L21	5.78366	0.00034	60	2.0		

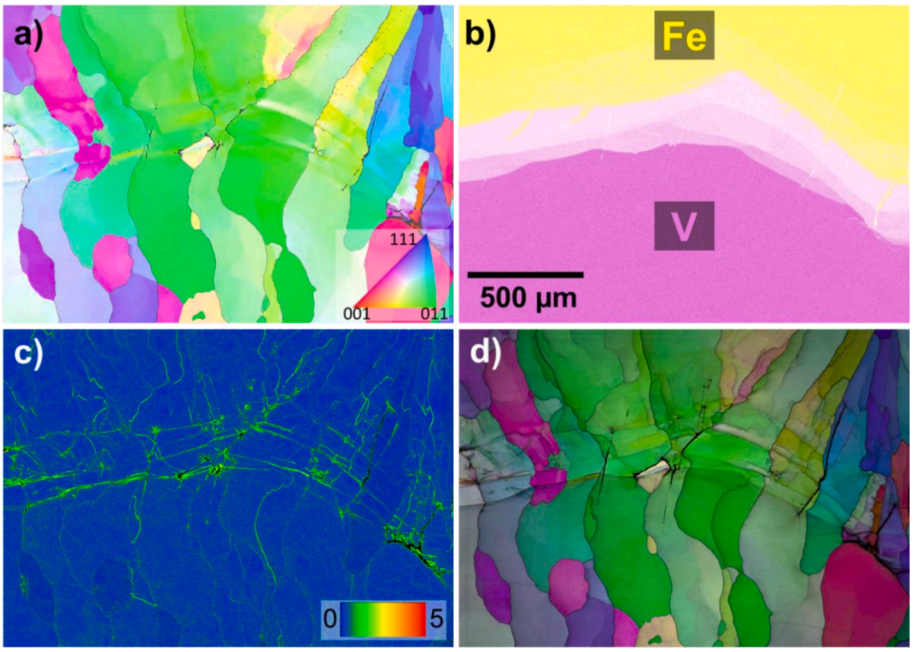

Fig. 7. LB-DED print of FeCrAl and VCrAl; a) IPF map; b) EDS map of Fe and V; c) KAM map; d) IQ + IPF map.

phases for further verification of the quaternary phase diagram of Fe-V-Cr-Al.

The synchrotron XRD results indicated a difference in microstructure between the annealed SPS and LB-DED samples, with no B2 phases in the former, while a small amount of B2 phase formation was found in the LB-DED sample. Ferreirós et al. found that the B2 phase only exists above 730 °C for the $Fe_{1-2x}V_xAl_x$ system, which would explain that a high temperature B2 phase, potentially formed during the SPS process, would have been dissolved into $L2_1$ and a bcc phase during annealing at 620 °C [29]. Rapid cooling during the LB-DED process would not provide sufficient time to eliminate the B2 phase completely. Higher micro-strain in the SPS sample, as shown in Table 3, even after an annealing is caused by the extensive $L2_1$ phase formation without cracking. The precipitate formation is visible with a very high density in Fig. 5. In the IPF and KAM maps of the LB-DED samples in Fig. 7, The stress accumulation through, but especially along the interface, indicated a pile up of stress caused by the sheet like formation of precipitates, and the intrinsic property differences between $L2_1$ and bcc matrix. Those micro strains in the lattice in the LB-DED sample have led to cracking at the interface as shown in Fig. 7. The observed susceptibility to cracking associated with the $L2_1$ phase formation and the resulting increase in microstrain aligns well with findings reported in previous studies [30,31].

Two design approaches can be considered to address the challenges at the Fe-V interface. Firstly, microstructural design through a deliberate in-situ $L2_1$ precipitation to form small precipitates (below 50 nm in diameter) has shown significant benefits in enhancing the strength of ferritic superalloys [32]. Diffusion kinetics can be tailored in other alloy systems, such as high entropy alloys, to control the growth rate of the $L2_1$ precipitates. Other researchers found the additions Hf or Nb helpful, as those elements were able to increase the energy of formation or reduce diffusion kinetics, preventing the formation of $L2_1$ or stabilizing it in a metastable state, respectively [33,34]. However, Nb is an element not suited for fusion system environments due to transmutation into long-activation elements [35]. For the Fe and V alloy interfaces, detailed thermodynamic calculations and experimental investigations regarding alloying compositions and cooling rates are necessary to achieve a sparse, finely dispersed $L2_1$ phase or to prevent its formation entirely. Secondly, alternative compositional pathways can be identified based on the latest insights into the Fe-V-Cr-Al quaternary phase diagram.

Recently, a hardness increase was also reported for stacked multi-material systems fabricated by LB-DED, which makes the SPS results relevant and applicable to the actual manufacturing of components with Fe-V interfaces [13]. The LB-DED process, characterized by rapid cooling rates on the order of 10^3–10^4 °C/s (depending on the material and processing parameters), significantly reduces the likelihood of σ-phase formation due to its sluggish formation kinetics and the presence of Al, an effective σ-phase suppressant [36]. Thus, as proven by the XRD synchrotron results, the cracking at the interface of the LB-DED fabricated sample in Fig. 7 can be attributed to the presence of a high temperature B2 and the $L2_1$ phases, both known for fast formation kinetics. From an additive manufacturing perspective, an $L2_1$ phase formation appears more detrimental than the formation of a potential σ phase. On the other hand, from a neutron irradiation perspective, the formation of the $L2_1$ phase could potentially be helpful, due to its exceptional

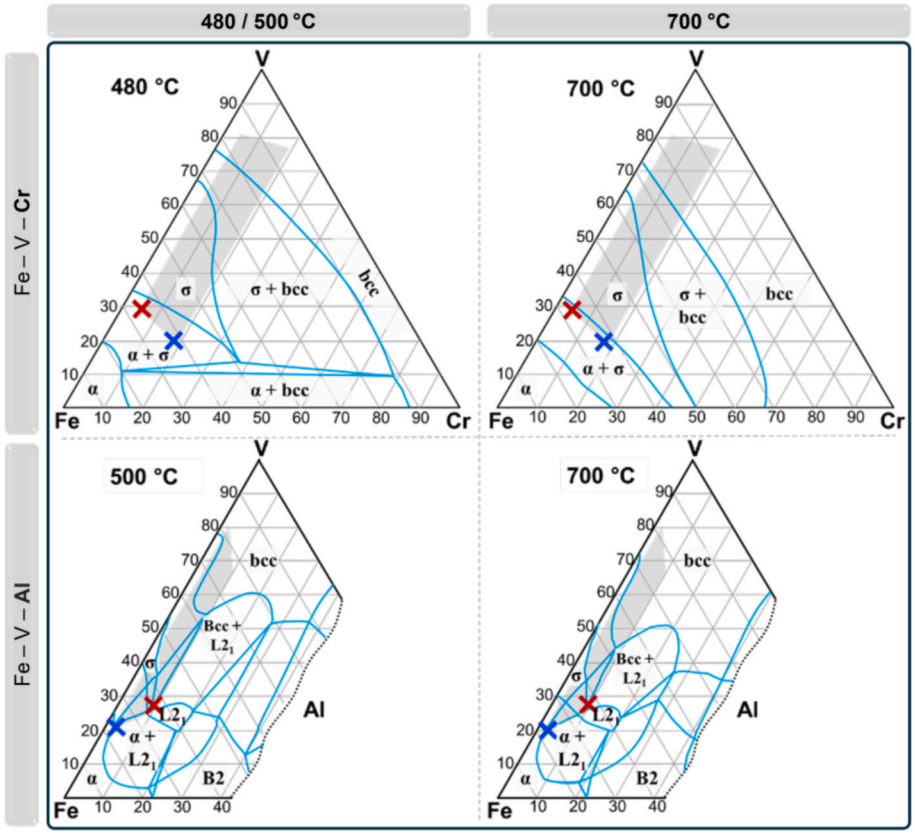

Fig. 8. Fe-V-Cr (top row) and cropped Fe-V-Al (bottom row) ternary phase diagrams at 480 (500) °C and 700 °C with the gray area representing the measured chemical compositions within the TEM lamella ([]). The blue and red crosses represent the 2-phase chemical compositions found in the lamella shown in adapted from 26–28Fig. 5.

resistance to radiation-induced hardening [32]. However, a crack-free manufacturing process is a key requirement for any material system, indicating an optimization of the chemical composition and processing. Diffusion simulations have been performed in a previous publication but were limited to the diffusion kinetics of the SPS sample. Future approaches should include the Lattice Boltzmann Method (LBM), a rapidly evolving numerical approach for modeling fluid flow and heat transfer within the melt pool. For the present multi material system, the challenging heat transfer and phase transitions during rapid solidification need to be considered in the simulation and are efforts out of scope for this manuscript.

Beyond the alloying and cooling optimization strategies, an alternative mitigation approach involving a modified compositional pathway has been developed and is proposed in Fig. 9, aiming to achieve an intermetallic-free interface. This approach is illustrated by three ternary phase diagrams at 620 °C, highlighting a feasible compositional pathway. By inserting a discrete pure Cr interlayer between VCrAl and FeCrAl, the formation of the $L2_1$ phase can be prevented, potentially enabling a crack-free transition between the two alloys. This proposed mitigation strategy is applicable to LB-DED manufacturing but may

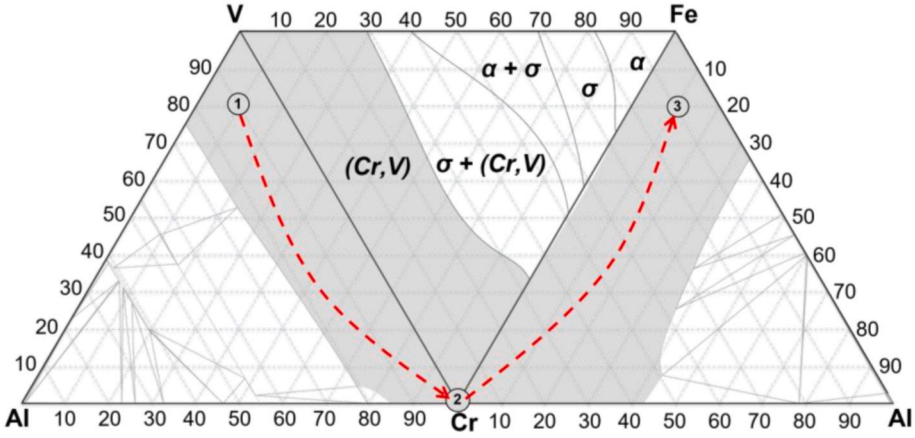

Fig. 9. Modified transition pathway from VCrAl to FeCrAl with a discrete Cr interlayer, marked with circles 1, 3, and 2 respectively. V-Cr-Al (left), Fe-V-Cr (middle) and Fe-Cr-Al (right) isotherms are simulated for 620 °C. Single phase bcc regions are marked with light gray. A potential transition pathway is highlighted with dashed red lines.

introduce long-term stability concerns. Preliminary LB-DED experiments incorporating a Cr interlayer between VCrAl and FeCrAl have been performed without exhibiting cracking. The characterization is ongoing in as-printed condition and will be followed by long-term thermal cycling tests to investigate the potential formation of a σ phase at lower temperatures. This study will be published in the near future. Nevertheless, further research and additional experimental data in the Fe-V-Cr-Al alloy system are necessary to refine thermodynamic simulations and optimize compositional gradient pathways between Fe and V alloys. The production of complex geometries for plasma facing components in a fusion reactor will require the transition layer design applied by additive manufacturing. Even though SPS cannot be used to manufacture complex structures with integrated cooling channels, the lessons learned from the annealed SPS samples are valuable to guide the DED process and the alloy design optimization.

5. Summary and conclusions

In the present study, the interface between FeCrAl and VCrAl was studied, and compositional gradient pathways were designed to prevent the formation of brittle intermetallic phases in the plasma-facing component temperature range of 550–1100 °C. Both the literature and the present results indicate that the complex Fe-V-Cr-Al system is not well understood and only partly experimentally explored. The work herein performed on annealed SPS samples and LB-DED samples led to the following conclusions:

- The enhancement of mechanical properties at the FeCrAl to VCrAl interface is directly related to significant intermetallic formation, specifically the $L2_1$ phase.
- A B2 phase was only observed in the LB-DED sample, while the $L2_1$ phase was identified in both samples.
- Annealing at 620 °C revealed no σ phase formation, potentially due to an increased Al content.
- More research on the Fe-V-Al-Cr system is necessary to develop validated strategies for bonding Fe-based and V-based alloys, which is critical for fusion system applications.
- Introducing a Cr buffer layer between FeCrAl and VCrAl is proposed as an easily implementable strategy during LB-DED additive manufacturing and is expected to result in a crack-free transition layer between these two alloys, as supported by the most recent Fe-V-Al-Cr phase diagram.

CRediT authorship contribution statement

Tim Gräning: Writing – review & editing, Writing – original draft, Visualization, Validation, Investigation, Formal analysis, Data curation, Conceptualization. **Deniz Ebeperi:** Writing – review & editing, Writing – original draft, Visualization, Investigation, Data curation. **Ibrahim Karaman:** Writing – review & editing, Supervision, Funding acquisition. **Ishtiaque Robin:** Writing – review & editing, Investigation. **Mobashera Saima Haque:** Writing – review & editing, Investigation, Formal analysis. **Akhil Kolanti:** Writing – review & editing, Investigation, Formal analysis. **David Sprouster:** Writing – review & editing, Supervision, Investigation, Formal analysis. **Lance Snead:** Writing – review & editing, Supervision. **Yutai Katoh:** Writing – review & editing, Supervision, Funding acquisition.

Declaration of competing interest

The authors declare that they have no known competing financial interests or personal relationships that could have appeared to influence the work reported in this paper.

Acknowledgement

This manuscript has been authored by UT-Battelle, LLC under Contract No. DE-AC05-00OR22725 with the U.S. Department of Energy. The United States Government retains and the publisher, by accepting the article for publication, acknowledges that the United States Government retains a non-exclusive, paid-up, irrevocable, world-wide license to publish or reproduce the published form of this manuscript, or allow others to do so, for United States Government purposes. The Department of Energy will provide public access to these results of federally sponsored research in accordance with the DOE Public Access Plan(http://energy.gov/downloads/doe-public-access-plan). Additional support is provided by U.S. Department of Energy (DOE), Advanced Research Projects Agency – Energy (ARPA-E) under Award Number 20/CJ000/08/03 at Oak Ridge National Laboratory.

These experiments were supported by the U.S. Department of Energy Office of Fusion Energy Sciences under contract DE-SC0018322 with the Research Foundation for the State University of New York at Stony Brook. This research used resources at the Pair Distribution Function Beamline of the National Synchrotron Light Source II, a U.S. Department of Energy (DOE) Office of Science User Facility operated for the DOE Office of Science by Brookhaven National Laboratory under Contract No. DE-SC0012704.

The research at Texas A&M University was supported by the Advanced Research Projects Agency - Energy (ARPA-E), U.S. Department of Energy under the Award number DE-AR0001370 (GAMOW Program) and DE-AR0001988 (CHADWICK Program). The authors want to thank the internal reviewer Yan-Ru Lin and Gabe Parker.

Data availability

Data will be made available on request.

References

[1] C. Bonnekoh, P. Lied, S. Zaefferer, U. Jäntsch, A. Hoffmann, J. Reiser, M. Rieth, The brittle-to-ductile transition in cold-rolled tungsten sheets: Contributions of grain and subgrain boundaries to the enhanced ductility after pre-deformation, Nucl. Mater. Energy 25 (2020) 100769, https://doi.org/10.1016/j.nme.2020.100769.

[2] S. Wurster, N. Baluc, M. Battabyal, T. Crosby, J. Du, C. García-Rosales, A. Hasegawa, A. Hoffmann, A. Kimura, H. Kurishita, R.J. Kurtz, H. Li, S. Noh, J. Reiser, J. Riesch, M. Rieth, W. Setyawan, M. Walter, J.-H. You, R. Pippan, Recent progress in R&D on tungsten alloys for divertor structural and plasma facing materials, J. Nucl. Mater. 442 (2013) S181–S189, https://doi.org/10.1016/j.jnucmat.2013.02.074.

[3] Ch. Linsmeier, M. Rieth, J. Aktaa, T. Chikada, A. Hoffmann, J. Hoffmann, A. Houben, H. Kurishita, X. Jin, M. Li, A. Litnovsky, S. Matsuo, A. von Müller, V. Nikolic, T. Palacios, R. Pippan, D. Qu, J. Reiser, J. Riesch, T. Shikama, R. Stieglitz, T. Weber, S. Wurster, J.-H. You, Z. Zhou, Development of advanced high heat flux and plasma-facing materials, Nucl. Fusion 57 (2017) 092007, https://doi.org/10.1088/1741-4326/aa6f71.

[4] V. Philipps, Tungsten as material for plasma-facing components in fusion devices, J. Nucl. Mater. 415 (2011) S2–S9, https://doi.org/10.1016/j.jnucmat.2011.01.110.

[5] S. Wang, J. Li, Y. Wang, X. Zhang, R. Wang, Y. Wang, J. Cao, Thermal damage of tungsten-armored plasma-facing components under high heat flux loads, Sci. Rep. 10 (2020) 1359, https://doi.org/10.1038/s41598-020-57852-8.

[6] J. Reiser, L. Garrison, H. Greuner, J. Hoffmann, T. Weingärtner, U. Jäntsch, M. Klimenkov, P. Franke, S. Bonk, C. Bonnekoh, S. Sickinger, S. Baumgärtner, D. Bolich, M. Hoffmann, R. Ziegler, J. Konrad, J. Hohe, A. Hoffmann, T. Mrotzek, M. Seiss, M. Rieth, A. Möslang, Ductilisation of tungsten (W): Tungsten laminated composites, Int. J. Refract. Met. Hard Mater 69 (2017) 66–109, https://doi.org/10.1016/j.ijrmhm.2017.07.013.

[7] J. Reiser, M. Rieth, A. Möslang, H. Greuner, D.E.J. Armstrong, T. Denk, T. Gräning, W. Hering, A. Hoffmann, J. Hoffmann, H. Leiste, T. Mrotzek, R. Pippan, W. Schulmeyer, T. Weingärtner, A. Zabernig, Tungsten (W) Laminate pipes for innovative high temperature energy conversion systems, Adv. Eng. Mater. 17 (2015) 491–501, https://doi.org/10.1002/adem.201400204.

[8] R. Subramanian, H. Tripathy, A.K. Rai, R.N. Hajra, S. Saibaba, T. Jayakumar, E. Rajendra Kumar, Thermal expansion characteristics of Fe–9Cr–0.12C–0.56Mn–0.24V–1.38W–0.06Ta (wt.%) reduced activation ferritic–martensitic steel, Journal of Nuclear Materials 459 (2015) 150–158, https://doi.org/10.1016/j.jnucmat.2015.01.026.

[9] H. Okamoto, Supplemental Literature Review of Binary phase Diagrams: B-Fe, Cr-Zr, Fe-Np, Fe-W, Fe-Zn, Ge-Ni, La-Sn, La-Ti, La-Zr, Li-Sn, Mn-S, and Nb-Re, J. Phase Equilib. Diffus. 37 (2016) 621–634, https://doi.org/10.1007/s11669-016-0465-z.
[10] S.-H. Lee, J.-H. Koo, O. Cakmak, J.-W. Cho, Effect of laser power during laser powder bed fusion on microstructure of joining interface between Tungsten and AISI 316L steel, Addit. Manuf. Lett. 11 (2024) 100246, https://doi.org/10.1016/j.addlet.2024.100246.
[11] T. Gräning, L. Tan, I. Robin, Y. Katoh, Y. Yang, A novel design of transitional layer structure between reduced activation ferritic martensitic steels and tungsten for plasma facing materials, J. Mater. Res. Technol. 24 (2023) 4285–4299, https://doi.org/10.1016/j.jmrt.2023.04.019.
[12] I.K. Robin, T. Gräning, Y. Yang, Y. Katoh, S.J. Zinkle, Microstructure and thermal stability of a structurally graded tungsten and reduced activation ferritic/martensitic steel joint, J. Mater. Res. Technol. 30 (2024) 3663–3674, https://doi.org/10.1016/j.jmrt.2024.04.087.
[13] D. Ebeperi, T. Graening, Y. Yang, A. Whitt, R. Seede, K.C. Atli, Y. Katoh, R. Arroyave, I. Karaman, Directed energy deposition of functionally graded V-4Cr-4Ti to Fe-9Cr transition for fusion power systems, Mater. Des. 254 (2025) 113979, https://doi.org/10.1016/j.matdes.2025.113979.
[14] M.W. Vaughan, M. Elverud, J. Ye, R. Seede, S. Gibbons, P. Flater, B. Gaskey, R. Arroyave, A. Elwany, I. Karaman, Development of a process optimization framework for fabricating fully dense advanced high strength steels using laser directed energy deposition, Addit. Manuf. 67 (2023) 103489, https://doi.org/10.1016/j.addma.2023.103489.
[15] R. Sarkar, C. Rentenberger, J. Rajagopalan, Electron Beam Induced Artifacts during in situ TEM Deformation of Nanostructured Metals, Sci. Rep. 5 (2015) 16345, https://doi.org/10.1038/srep16345.
[16] K. Kese, P.A.T. Olsson, A.-M. Alvarez Holston, E. Broitman, High temperature nanoindentation hardness and Young's modulus measurement in a neutron-irradiated fuel cladding material, Journal of Nuclear Materials 487 (2017) 113–120, https://doi.org/10.1016/j.jnucmat.2017.02.014.
[17] J. Ilavsky, Nika: software for two-dimensional data reduction, J. Appl. Crystallogr. 45 (2012) 324–328, https://doi.org/10.1107/S0021889812004037.
[18] L. Lutterotti, Maud: a Rietveld analysis program designed for the internet and experiment integration, Acta Crystallogr. A: Found. Crystallogr. 56 (2000) s54–s, https://doi.org/10.1107/S0108767300021954.
[19] Y. Liu, H. Liu, C. Fan, W. Bin, L. Zhang, Crystal structure of $AlFe_{0.95}$, IUCrData 8 (2023) x231065, https://doi.org/10.1107/S2414314623010659.
[20] J.-I. Seki, M. Hagiwara, T. Suzuki, Metastable order-disorder transition and sigma phase formation in Fe-V binary alloys, J. Mater. Sci. 14 (1979) 2404–2410, https://doi.org/10.1007/BF00737030.
[21] G. Bergman, D.P. Shoemaker, The determination of the crystal structure of the σ phase in the iron–chromium and iron–molybdenum systems, Acta Cryst 7 (1954) 857–865, https://doi.org/10.1107/S0365110X54002605.
[22] A.M. Van der Kraan, K.H.J. Buschow, The 57Fe Mössbauer isomer shift in intermetallic compounds of iron, Physica B+c 138 (1986) 55–62, https://doi.org/10.1016/0378-4363(86)90492-4.
[23] J.J. Bara, B.F. Bogacz, T. Rendecki, W. Zarek, The crystal structure and magnetic properties of cold-worked (FexV1−x)3Al alloys, J. Magn. Magn. Mater. 59 (1986) 208–214, https://doi.org/10.1016/0304-8853(86)90414-2.
[24] O. Crisan, A.D. Crisan, Phase transformation and exchange bias effects in mechanically alloyed Fe/magnetite powders, J. Alloy. Compd. 509 (2011) 6522–6527, https://doi.org/10.1016/j.jallcom.2011.03.147.
[25] P. Karen, E. Suard, F. Fauth, Crystal Structure of Stoichiometric $YBa_2Fe_3O_8$, Inorg. Chem. 44 (2005) 8170–8172, https://doi.org/10.1021/ic048746b.
[26] J. Wang, Q. Feng, S. Wang, X. Lu, C. Li, Thermodynamic modeling of Al–Fe–V ternary system, Mater. Res. Express 6 (2019) 126539, https://doi.org/10.1088/2053-1591/ab55a6.
[27] B.-J. Lee, D.N. Lee, A thermodynamic evaluation of the Fe-Cr-V-C system, JPE 13 (1992) 349–364, https://doi.org/10.1007/BF02674980.
[28] V. Ivanchenko and Tetyana Pryadko, M. Materials Science International Team, G. Effenberg, Cr-Fe-V Ternary Phase Diagram Evaluation · Phase diagrams, crystallographic and thermodynamic data: Datasheet from MSI Eureka in SpringerMaterials (https://materials.springer.com/msi/docs/sm_msi_r_10_014713_01), (n.d.). https://materials.springer.com/msi/docs/sm_msi_r_10_014713_01.
[29] P.A. Ferreirós, P.R. Alonso, P.H. Gargano, P.B. Bozzano, H.E. Troiani, A. Baruj, G. H. Rubiolo, Characterization of microstructures and age hardening of Fe1−2xAlxVx alloys, Intermetallics 50 (2014) 65–78, https://doi.org/10.1016/j.intermet.2014.02.014.
[30] S.A. Azmi, A. Michalcová, L. Senčekova, M. Palm, Microstructure and mechanical properties of Fe-Al-Nb-B alloys, MRS Adv. 2 (2017) 1353–1359, https://doi.org/10.1557/adv.2017.138.
[31] X. Chen, S. Peng, Y. Liu, S. Bai, L. Zhang, S. He, O.I. Gorbatov, X. Qu, Ductility deterioration induced by L21 phase in ferritic alloy through Ti addition, J. Mater. Res. Technol. 25 (2023) 3273–3284, https://doi.org/10.1016/j.jmrt.2023.06.176.
[32] K. Ma, P.A. Ferreirós, T.W. Pfeifer, R.G. Abernethy, S. von Tiedemann, N. Peng, G. Greaves, C. Ophus, K. Sun, A.H. Mir, L. Wang, S. Huang, S. Zhao, P.E. Hopkins, C.D. Hardie, A.J. Knowles, Intermetallic dispersion-strengthened ferritic superalloys with exceptional resistance to radiation-induced hardening, Acta Mater. 293 (2025) 121095, https://doi.org/10.1016/j.actamat.2025.121095.
[33] M. Kim, A.J. Freeman, S. Kim, J.H. Perepezko, G.B. Olson, Phase stability of the intermetallic L21 Heusler alloys of A2(Hf1−xZrx)Al (where A=Pd and Pt) for an Nb-based high-temperature materials design, Appl. Phys. Lett. 87 (2005) 261908, https://doi.org/10.1063/1.2136223.
[34] A. Gedsun, F. Stein, M. Palm, Phase Equilibria in the Fe-Al-Nb(-B) system at 700 °C, J. Phase Equilib. Diffus. 43 (2022) 409–418, https://doi.org/10.1007/s11669-022-00979-0.
[35] M.R. Gilbert, J.C. Sublet, R.A. Forrest, C.C. for F. Energy, Handbook of Activation, Transmutation, and Radiation Damage Properties of the Elements Simulated Using FISPACT-II & TENDL-2014 ; Magnetic Fusion Plants, Culham Centre for Fusion Energy, 2015. https://books.google.com/books?id=ztw5zQEACAAJ.
[36] J. Jeong, S. Webster, S. Liao, J.-E. Mogonye, K. Ehmann, J. Cao, Cooling rate measurement in directed energy deposition using photodiode-based planck thermometry (PDPT), Addit. Manuf. Lett. 3 (2022) 100101, https://doi.org/10.1016/j.addlet.2022.100101.